Journal of Systems Engineering and Electronics
Vol. 32, No. 4, August 2021, pp.822 – 830

Suppression of the G-sensitive drift of laser gyro in dual-axis rotational inertial navigation system

YU Xudong*, WANG Zichao, FAN Huiying, WEI Guo, and WANG Lin

College of Advanced Interdisciplinary Studies, National University of Defense Technology, Changsha 410073, China

Abstract: The dual-axis rotational inertial navigation system (INS) with dithered ring laser gyro (DRLG) is widely used in high precision navigation. The major inertial sensor errors such as drift errors of gyro and accelerometer can be averaged out, but the G-sensitive drifts of laser gyro cannot be averaged out by indexing. A 16-position rotational simulation experiment proves the G-sensitive drift will affect the long-term navigation error for the rotational INS quantitatively. The vibration coupling and asymmetric structure of the DRLG are the main errors. A new dithered mechanism and optimized DRLG is designed. The validity and efficiency of the optimized design are conformed by 1 *g* sinusoidal vibration experiments. An optimized inertial measurement unit (IMU) is formulated and measured experimentally. Laboratory and vehicle experimental results show that the divergence speed of longitude errors can be effectively slowed down in the optimized IMU. In long term independent navigation, the position accuracy of dual-axis rotational INS is improved close to 50%, and the G-sensitive drifts of laser gyro in the optimized IMU are less than 0.000 2 °/h. These results have important theoretical significance and practical value for improving the structural dynamic characteristics of DRLG INS, especially the high-precision inertial system.

Keywords: inertial navigation, rotational inertial navigation system (INS), laser gyro, G-sensitive drift.

DOI: 10.23919/JSEE.2021.000071

1. Introduction

Strapdown inertial navigation system (INS) is the core instrument for precise guidance and attitude control of aircraft, ships, submarines, spacecrafts, missiles, and others [1,2]. In the INS, the attitude is measured by integrating gyros, and the velocity and position are measured by integrating accelerometers. A small error generated by the inertial sensor will be converted into a large navigation error by integrating. Therefore, many methods are proposed to reduce inertial sensor errors.

On the basis of strapdown inertial navigation and rotation technology, a new INS called rotational INS is proposed [3,4]. In dual-axis rotational INS, the inertial measurement unit (IMU) rotates around the azimuth axis and the roll axis. The major inertial sensor errors, such as constant gyro drift errors, constant accelerometer drift errors, installation errors, and scale factor errors, will be averaged out in every few minutes [5].

Many multi-position rotation schemes are proposed to compensate the inertial sensor errors, such as the 8-position scheme, the 16-position scheme, and the 64-position scheme [6−8]. Kalman filters are performed to self-calibrate various gyro and accelerometer misalignments and scale-factors in dual-axis rotational INS [9−12]. These error sources are observable because of the rotational motion. At the same time, rotation also brings some new navigation errors [5]. Under the influence of gravity, the gyro drift changes as IMU rotates up and down in inertial space. The uncertainty error of the gyro drift caused by rotation is defined as the G-sensitive drift. The G-sensitive drift is difficult to calibrate accurately through the precise turntable. In [13,14], self-calibration methods by the Kalman filter were proposed to calibrate the G-sensitive drift in dual-axis rotational INS. These methods can compensate the G-sensitive drift, but the best technical solution is to find out the source of error and control it.

The present paper is organized as follows. In Section 2, the error propagation characteristics of the G-sensitive drift in dual-axis rotational INS are quantitatively discussed. In Section 3, the error mechanism of the G-sensitive drift is presented and the deformation law of cavity optical path is given. In Section 4, based on the finite element method, an optimized design of DRLG for dual-axis rotational INS is analyzed. The validity and efficiency of the optimized design will be confirmed by 1 *g* sinusoidal vibration experiments. In Section 5, we compare the existing structure and the optimized IMU with the dual-axis rotational navigation experiments. Finally, Section 6 presents the conclusions.

Manuscript received November 12, 2020.
*Corresponding author.
This work was supported by the National Natural Science Foundation of China (61503399).

2. Error propagation of the G-sensitive drift

Error propagation equations of the dual-axis rotational INS are as follows:

$$\dot{\boldsymbol{\phi}}^n = -(\boldsymbol{\omega}_{ie}^n + \boldsymbol{\omega}_{en}^n)\times\boldsymbol{\phi}^n + \delta\boldsymbol{\omega}_{in}^n - \boldsymbol{C}_b^n\boldsymbol{\varepsilon}^b, \tag{1}$$

$$\delta\dot{\boldsymbol{v}}^n = \boldsymbol{f}^n\times\boldsymbol{\phi}^n - (2\boldsymbol{\omega}_{ie}^n + \boldsymbol{\omega}_{en}^n)\times\delta\boldsymbol{v}^n - (2\delta\boldsymbol{\omega}_{ie}^n + \boldsymbol{\omega}_{en}^n)\times\boldsymbol{v}^n + \delta\boldsymbol{g}^n + \boldsymbol{C}_b^n\nabla^b, \tag{2}$$

$$\delta\dot{\boldsymbol{r}}^n = -\boldsymbol{\omega}_{en}^n\times\delta\boldsymbol{r}^n + \delta\boldsymbol{v}^n, \tag{3}$$

where n, b, i, and e represent the navigation frame, the body frame, the inertia frame, and the earth frame respectively. The superscript of a vector indicates the frame to which the vector is projected. $\boldsymbol{\phi}^n$, $\delta\boldsymbol{v}^n$, and $\delta\boldsymbol{r}^n$ are respectively the phi-angle error (attitude error), the velocity error, and the position error. $\boldsymbol{f}^n$ is the force vector sensed by the space coordinate axis of the accelerometer; g is the gravity; $\boldsymbol{\omega}$ is the angular rate vector sensed by the space coordinate axis of the gyro; $\delta\boldsymbol{\omega}$ is the angular rate error. The sign "×" means taking the cross product of the two vectors; $\boldsymbol{C}_b^n$ is the direction cosine matrix; $\boldsymbol{\varepsilon}^b$ is the gyroscope drift error; ∇^b is the accelerometer drift error.

The IMU errors in this paper include constant drifts, G-sensitive drifts, scale factor errors and misalignment errors. The IMU error model is given as follows:

$$\boldsymbol{\varepsilon}^b = \boldsymbol{b}_g + \boldsymbol{b}_g^{f^b} + \boldsymbol{S}_g\boldsymbol{\omega}_{ib}^g + \boldsymbol{M}_g^b\boldsymbol{\omega}_{ib}^g + \boldsymbol{v}_g, \tag{4}$$

$$\nabla^b = \boldsymbol{b}_a + \boldsymbol{S}_a\boldsymbol{f}^a + \boldsymbol{M}_a^b\boldsymbol{f}^a + \boldsymbol{v}_a, \tag{5}$$

where $\boldsymbol{b}_g$ and $\boldsymbol{b}_a$ are constant drifts; $\boldsymbol{b}_g^{f^b}$ is G-sensitive drift; $\boldsymbol{S}_g$ and $\boldsymbol{S}_a$ are scale factor errors; $\boldsymbol{M}_g^b$ and $\boldsymbol{M}_a^b$ are misalignment errors; $\boldsymbol{v}_g$ and $\boldsymbol{v}_a$ are measurement noises.

The azimuth axis is defined as the U-axis (vertical rotation axis) and the East axis is defined as the E-axis (horizontal rotation axis). The rotation scheme adopts the 16-position rotation scheme [7], as shown in Fig.1.

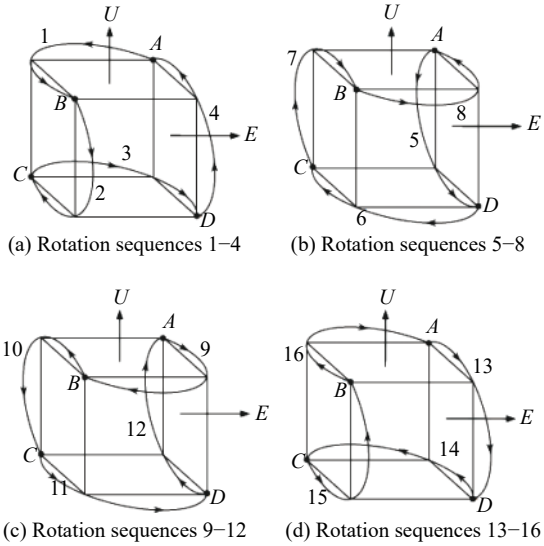

(a) Rotation sequences 1−4 (b) Rotation sequences 5−8

(c) Rotation sequences 9−12 (d) Rotation sequences 13−16

Fig. 1 16-position rotation scheme

Based on the IMU error model, the average results of the G-sensitive drift in dual-axis rotational INS can be divided into Z-axis rotation and X-axis rotation. The G-sensitive drift is as follows:

$$\boldsymbol{b}_g^{f^b} = \begin{bmatrix} b_x\cdot\mathrm{sign}(f^{bx}) \\ b_y\cdot\mathrm{sign}(f^{by}) \\ b_z\cdot\mathrm{sign}(f^{bz}) \end{bmatrix} \tag{6}$$

where $\mathrm{sign}(\boldsymbol{f}^b) = \begin{cases} +1, & \boldsymbol{f}^b \geqslant 0 \\ -1, & \boldsymbol{f}^b < 0 \end{cases}$, b_x, b_y, and b_z are constant drifts.

In the Z-axis rotation type with an angle of φ, the indexing mechanism rotation matrix can be written as

$$\boldsymbol{C}_b^n = \begin{bmatrix} \cos\varphi & 0 & -\sin\varphi \\ 0 & 1 & 0 \\ \sin\varphi & 0 & \cos\varphi \end{bmatrix}. \tag{7}$$

When the IMU rotates from 0° to 360° around the N-axis, the G-sensitive drift is as follows:

$$\int_0^T \boldsymbol{b}_g^n\mathrm{d}t = \int_0^T \boldsymbol{C}_b^n\boldsymbol{b}_g^{f^b}\mathrm{d}t = \int_0^T \begin{bmatrix} \cos\varphi & 0 & -\sin\varphi \\ 0 & 1 & 0 \\ \sin\varphi & 0 & \cos\varphi \end{bmatrix}\cdot$$

$$\begin{bmatrix} b_x^{f^b}\cdot\mathrm{sign}(f^{bx}) \\ b_y^{f^b}\cdot\mathrm{sign}(f^{by}) \\ b_z^{f^b}\cdot\mathrm{sign}(f^{bz}) \end{bmatrix}\mathrm{d}t = \begin{bmatrix} 0 \\ 4\varepsilon_y^b \\ 4(\varepsilon_x^b + 4\varepsilon_z^b) \end{bmatrix}. \tag{8}$$

The results show that the dual-axis rotation does not average the G-sensitive drift, but can be modulated to a constant within n frames.

A simulation by the 16-position rotation scheme is carried out to verify the theoretical analysis with the following conditions [7]: (i) the initial latitude is N28.222°; (ii) the rotation rate is 12 °/s; (iii) the stop time for each position is 30 s; (iv) the G-sensitive drift is set as 0.000 5 °/h; (v) the other errors are set as 0. The simulation results are shown in Fig.2.

The results show that the G-sensitive drift of the laser gyro is the main reason for the slope term of longitude error, and it increases linearly with time. When the G-sensitive drift of the laser gyro is set as 0.000 5 °/h, the longitude error increases to 0.42 nmiles during a 72 h independent inertial navigation. Therefore, the G-sensitive drift of the laser gyro is the main factor affecting the long time navigation, in order to improve navigation accuracy, the G-sensitive drift should be inhibited and compensated.

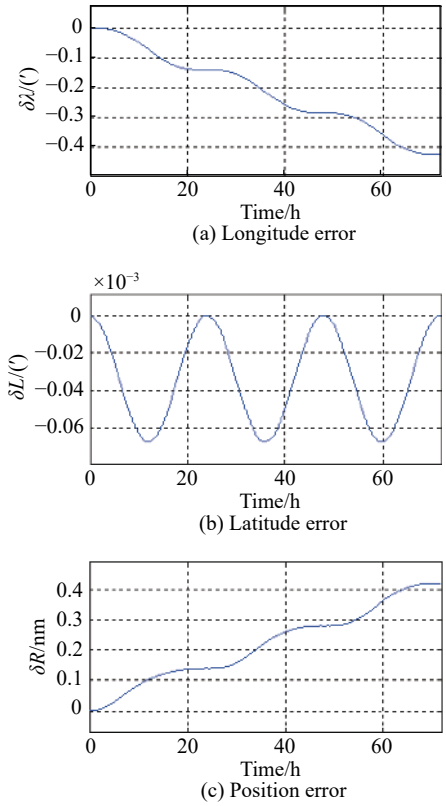

Fig. 2 Navigation error curves caused by the G-sensitive drift of laser gyro

3. Error analysis of G-sensitive drift

3.1 DRLG sturcture

DRLG is mainly composed of the ring resonator and the dither mechanism [15,16], as shown in Fig. 3. The ring resonator is made of glass ceramics with a low expansion coefficient, and the dither mechanism is mainly used to suppress the lock region of the gyroscope [17,18]. A simplified cross-section view of the installation mode between the glass cavity and the dither mechanism is shown in Fig. 4. The design of this installation method is mainly to control the influence of temperature on the shape change of the gyro cavity. At area A, a ring-shaped belt is used to connect the glass cavity and the dithering mechanism. Area B is the mounting area of the dithering mechanism and the mounting case.

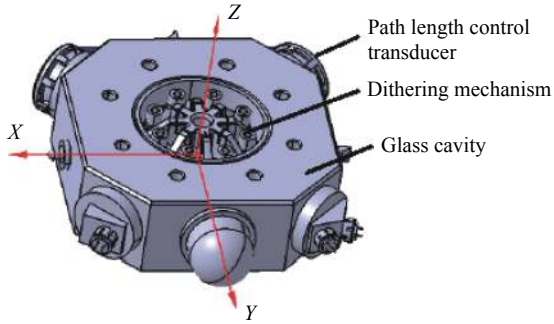

Fig. 3 Structure diagram of laser gyro

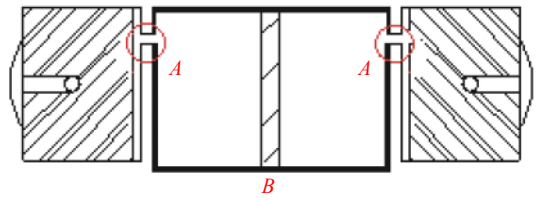

Fig. 4 Simplified cross-section view of installation mode along the *X* axis and the *Z* axis

3.2 Optical path deformation

In an ideal state, the spherical mirror and the planar mirror have no motion. At this point, the optical path inside the gyroscope passes through the hole and the central axis of the aperture to form a closed optical path. The resonator has the largest modal volume and the smallest cavity loss, and the gyro is in the best working state. Due to the asymmetric installation mode of the dither mechanism, gravity or external vibration will be transferred to the optical resonator through the dither mechanism when the gyro or the IMU is flipped. The length or coplanarity of the optical path and the position of the mirror will change, resulting in the change of the length or coplanarity of the cavity [19].

When spherical mirror or planar mirror is tilted, the light path will change, as shown in Fig. 5.

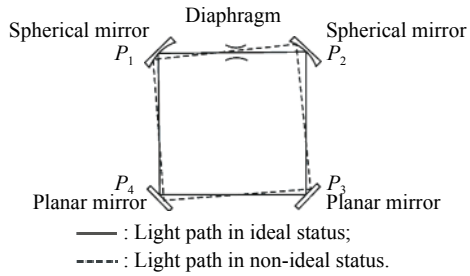

Fig. 5 Light change caused by light path variations

The total transformation matrix is as follows:

$$\boldsymbol{M} = \boldsymbol{TL}_{\text{half}} \times \boldsymbol{Mm}_1 \times \boldsymbol{TL}_4 \times \boldsymbol{Mm}_4 \times \boldsymbol{TL}_3 \times \boldsymbol{Mm}_3 \times \boldsymbol{TL}_2 \times \boldsymbol{Mm}_2 \times \boldsymbol{TL}_{\text{half}} \tag{9}$$

where $\boldsymbol{TL}_{\text{half}}$ is the propagator matrix from aperture to spherical mirror P_2, $\boldsymbol{Mm}_1$, $\boldsymbol{Mm}_2$, $\boldsymbol{Mm}_3$ and $\boldsymbol{Mm}_4$ represent the transformation matrix of the grooved mirror in P_1, P_2, P_3 and P_4, respectively, and $\boldsymbol{TL}_1$, $\boldsymbol{TL}_2$, $\boldsymbol{TL}_3$ and $\boldsymbol{TL}_4$ express the propagator matrix of light transmitting in four sides of quadrilateral cavity. When the matrix $\boldsymbol{M}$ is equal to 1, the resonant optical path is self-consistent, that is, the light propagates one circle in the resonant cavity and then coincides. After the light propagates in the resonator for one circle, the self-consistency of the optical path is

$$\begin{pmatrix} M_{11}-1 & M_{12} & M_{13} & M_{14} \\ M_{21} & M_{22}-1 & M_{23} & M_{24} \\ M_{31} & M_{32} & M_{33}-1 & M_{34} \\ M_{41} & M_{42} & M_{43} & M_{44}-1 \end{pmatrix} \begin{pmatrix} r_x \\ r_x' \\ r_y \\ r_y' \end{pmatrix} = -\begin{pmatrix} M_{15} \\ M_{25} \\ M_{35} \\ M_{45} \end{pmatrix} \tag{10}$$

where r_x, r_y are the distance from incident ray to the x and the y axis respectively, r_x' and r_y' represent the deflection angle of the incident light from the optical axis. By solving matrix equation (10), we can get the solution to r_x, r_x', r_y, and r_y'.

In order to ensure that the laser gyro works in a single mode state, a small diaphragm is usually set at the waist position of the Gauss beam in the ring resonator (shown in Fig. 5) to suppress the high-order transverse mode. However, the actual optical path is often not ideal through the center of the diaphragm. Fig. 6 is a schematic diagram of the offset of the actual optical path at the diaphragm relative to the ideal optical axis, where x_0 and y_0 represent the offset along the x-axis and y-axis respectively.

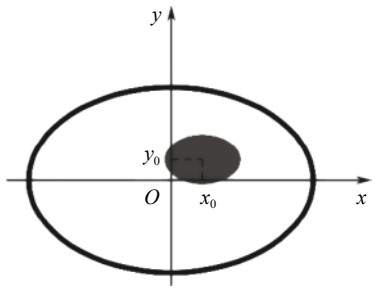

Fig. 6 Diagram of diaphragm and beam section

The diffractive loss of the diaphragm to the fundamental mode beam [20] is

$$\delta_{00} = 1 - \iint_S a_{00}^2 \mathrm{d}x\mathrm{d}y \tag{11}$$

where $a_{00} = \dfrac{1}{\sqrt{2/(\pi\sigma_x\sigma_y)}} \exp\left\{-\dfrac{(x-x_0)^2}{\sigma_x^2} - \dfrac{(y-y_0)^2}{\sigma_y^2}\right\}$ is the normalized amplitude of light field, σ_y and σ_y are the waist radii of Gaussian beam, and S is the aperture area surrounded by the diaphragm.

When a gyro or an IMU is flipped, the effect of gravity or external vibration on the resonator causes the spherical or planar mirror to deform or tilt [21,22]. It can be seen from (9) and (10) that the central position of the Gaussian beam will also change. The diffraction loss at the gyro diaphragm is changed and modulated. The accuracy or performance of gyroscopes will vary slightly. The reason for this change lies in the distortion of the gyro cavity, which mainly depends on the installation and connection mode of the gyro. From Fig. 4, we can see that the error source of the G-sensitive drift is the spatial asymmetry of gyro structure and the connection mode between the dithering mechanism and the laser cavity.

4. Optimization design of DRLG

4.1 Optimization analysis

An optimization scheme of the dither mechanism is given in this section, as shown in Fig.7. A simplified cross-section view of the installation mode between the glass cavity and the dither mechanism for the optimized structure is shown in Fig. 8. The connection mode of the dither mechanism and the cavity is mainly optimized. The connection mode is symmetrical from top to bottom, which is divided into 16 small contact surfaces to reduce the influence of temperature on the gyro cavity.

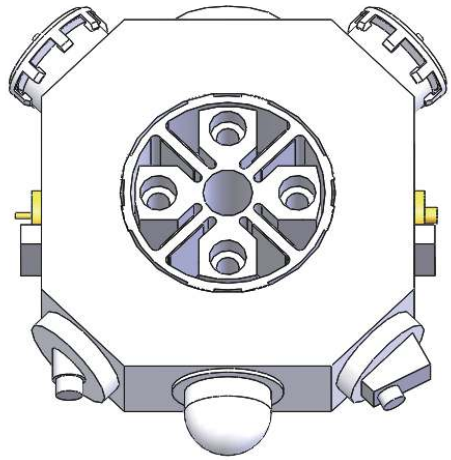

Fig. 7 Optimized DRLG

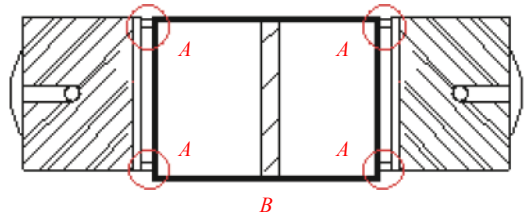

Fig. 8 Simplified cross-section view of installation mode for the optimized structure

The ANSYS software is used to analyze the static force of the existing structure and the optimized structure [23]. A finite element model is established, and 1 g gravity is applied on the gyro to compare and analyze the deformation of the cavity. Four typical nodes on the spherical mirror and the planar mirror are selected to measure the cavity size change of the existing structure and the optimized structure. The deformation results under 1 g gravity are shown in Fig. 9. The node deformation on the spheri-

cal mirror and the planar mirror obtained by simulation is substituted into (10) to calculate the change of the spot center position at the aperture along the X-axis and the Y-axis. According to (11), the diffraction loss of the resonator can be calculated, and the optimized diffraction loss can be reduced by 28% compared with the existing diffraction loss.

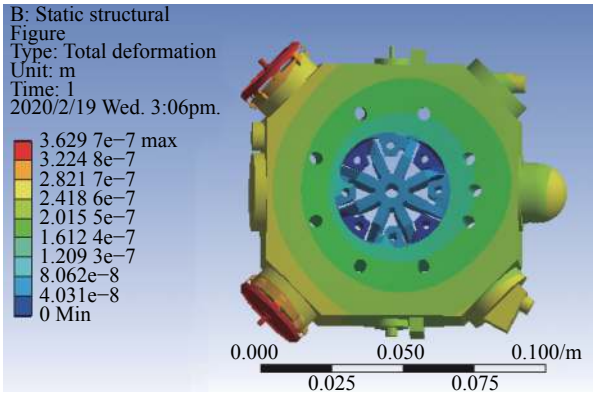

(a) Existing structure

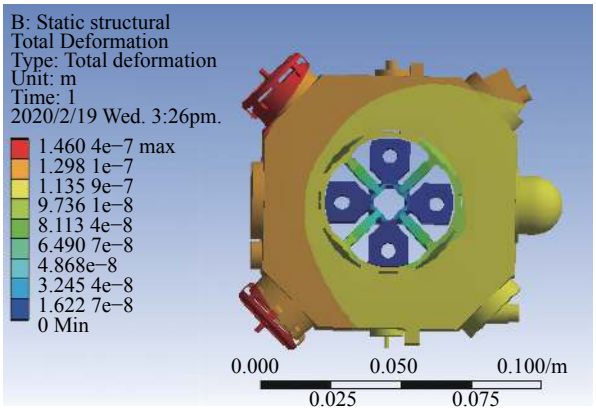

(b) Optimized structure

Fig. 9 Comparison of the deformation for the existing structure and the optimized structure

4.2 Sinusoidal vibration test

In order to verify the design and simulation results, sinusoidal vibration tests are carried out. The experimental apparatus of the sinusoidal vibration test is shown in Fig.10. Firstly, the acceleration sensors are mounted on the vibration table and the resonator cavity respectively. Then, the dithered ring laser gyro (DRLG) and the vibration table are powered on, and 1 g sine excitation force is imposed. Thirdly, we record the output amplitude of accelerometers and DRLG. The accelerometer mounted on the glass cavity is used to measure the acceleration response of the structure. Experimental apparatus of the DLRG is shown in Fig. 10.

Fig. 10 Acceleration response experiment for 1 g sinusoidal vibration input

Under the same test sequence, vibration tests are carried out on the existing DRLG and the optimized DRLG. The frequency range of the sinusoidal vibration test is 5 Hz to 1 000 Hz. The measured acceleration response spectrum is shown in Fig. 11. The frequencies of point 1 and point 2 of the existing DRLG correspond to the resonant mode frequencies respectively. At these points, the external vibration will be amplified by structural resonance, which will cause deformation of the cavity. For the optimized DRLG, there is almost no resonance amplification on the glass cavity from 5 Hz to 1 000 Hz.

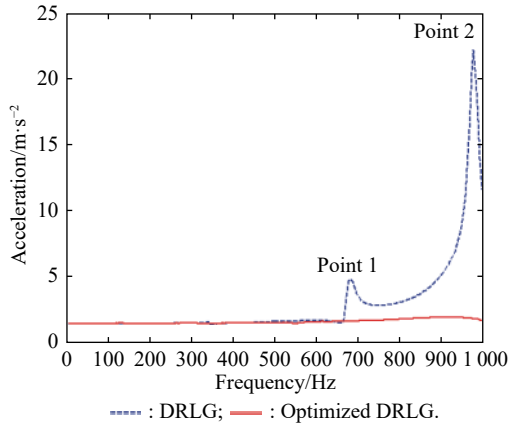

Fig. 11 Acceleration response of the existing DRLG and optimized DRLG for 1 g sinusoidal vibration

The outputs of the existing DRLG and the optimized DRLG are recorded while sinusoidal vibration tests are carried out. Firstly, let the gyros keep stationary for 120 s, then start the sinusoidal vibration test, and the test time is 200 s. Then keep them stationary for 120 s. The outputs of the two gyros are shown in Fig. 12. Sinusoidal vibra-

tion test shows that the optimized DRLG has a better anti-vibration capability and is more suitable for space reversal.

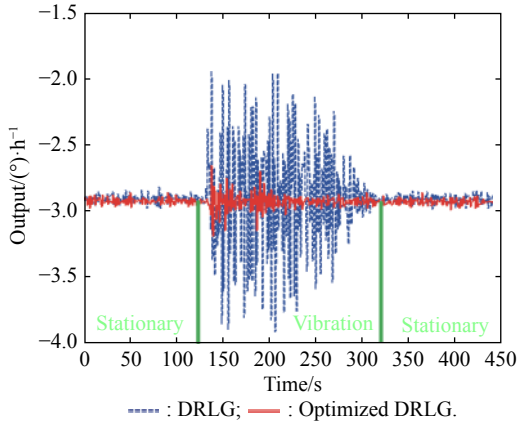

Fig. 12 Outputs of the DRLG for sinusoidal vibration test

5. Experiment and discussion

Because G-sensitive drift is very small, it cannot be accurately measured by turntable experiments, it can only be verified by navigation experiments. Laboratory experiments and vehicle experiments are carried out by using a dual-axis rotational INS. A dual-axis rotational INS includes a dual-axis rotational IMU, power supply, and a display and control panel as shown in Fig. 13. The 16-position rotation scheme presented in Section 2 is adopted. The IMU contains three laser gyros (0.005 °/h) and three quartz flexible accelerometers (10 μ*g*) [14].

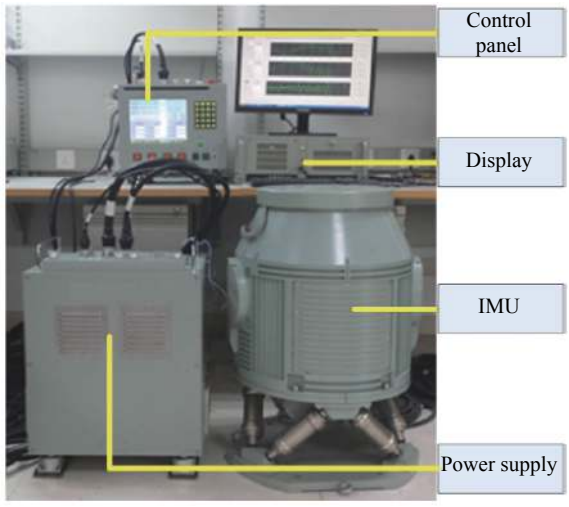

Fig. 13 A dual-axis rotational INS

For comparison, two dual-axis rotational INSs are manufactured which are defined as INS-A and INS-B. The INS-A and INS-B have the same power supply, display and control panel. The IMU in the two INSs is nearly the same except for the dither mechanism in the DRLG. The three existing DRLGs are used in INS-A, and the three optimized DRLGs are used in INS-B. Both the laboratory experiments and the vehicle experiments are performed with the same conditions.

Two groups of static tests are carried out in the laboratory tests, using 6 h of alignment and 120 h of static inertial navigation respectively. The position errors of INS-A and INS-B are shown in Fig. 14.

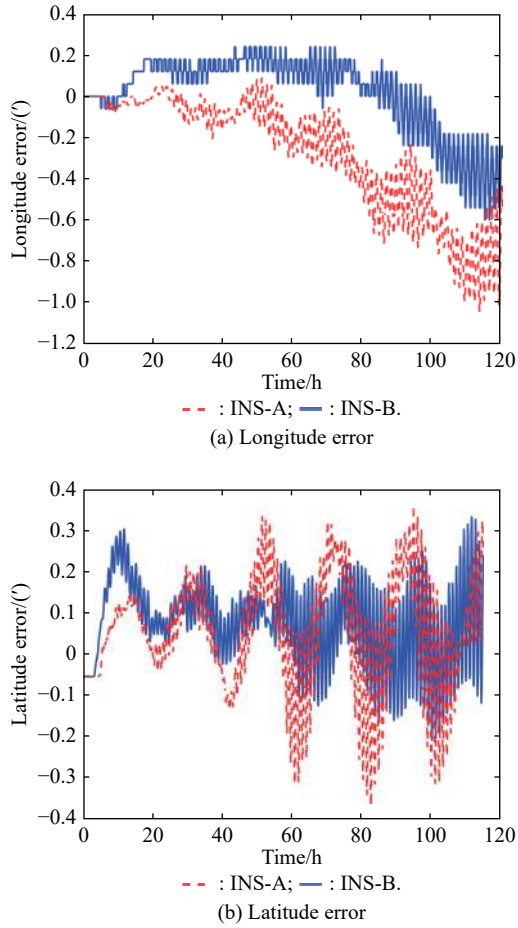

Fig. 14 Comparison of navigation errors before and after suppression of the G-sensitive drift in laboratory experiment

The results show that suppressing the G-sensitive drift can effectively reduce the divergence rate of longitude error. The maximum longitude error decreases from 1 nm to 0.6 nm within 120 h, which verifies the analysis results in Section 2 and Section 3.

According to (8), we can conclude that the G-sensitive drift of the optimized DRLG is less than 0.000 2 °/h.

Two sets of vehicle tests are carried out near 28.222° N. Both tests involved 6 h of alignment and 120 h of navigation. The vehicle experiments are carried out on the same

trajectories. The differential global position system (DGPS) information is used as the true value, and the longitude and latitude errors of INS-A and INS-B are shown in Fig. 15.

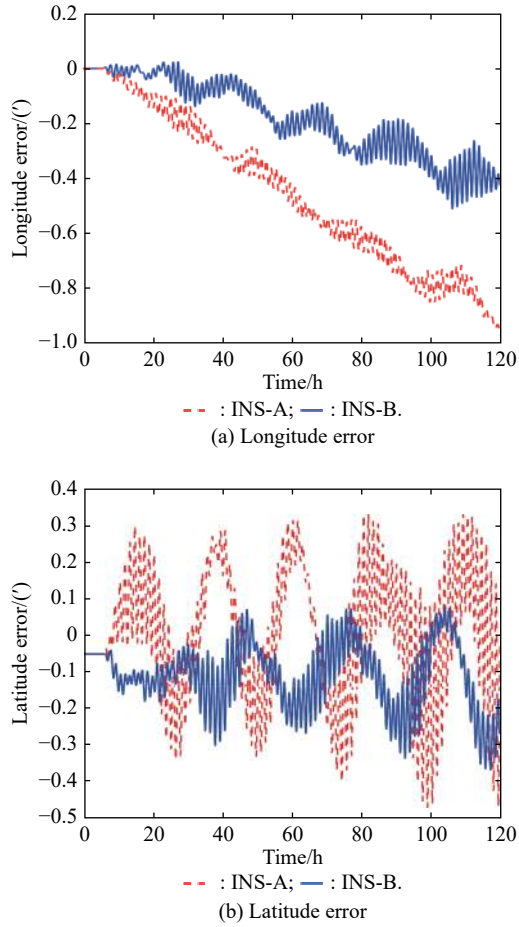

Fig. 15 Comparison of longitude and latitude errors before and after suppression of the G-sensitive drift in vehicle experiment

In the vehicle test, the longitude error is less than 0.4′ with the optimized DRLG, while the longitude error of INS-A rapidly diverges with time for the existing DRLG. We can conclude the navigation precision can be improved by suppressing the G-sensitive drift. The residual error of longitude is mainly caused by random walks.

In order to improve the reliability of the experiment, we conduct the same three sets of experiments within a period from May, 2020 to September, 2020. The experiments' results are listed in Table 1.

In Table 1, the longitude errors in INS-B are from 0.35′ to 0.52′, and the longitude errors in INS-A are from 0.87′ to 1.23′, whereas, the mean value are 0.45′ and 1′ respectively. And the latitude errors, east velocity errors and north velocity errors in INS-A are similar with those in INS-B. From the longitude errors in the laboratory experiment, the vehicle experiment and the repetitive experiment, we can conclude that the G-sensitive drift of the optimized DRLG is less than 0.000 2 °/h. The navigation results obtained by using the optimized DRLG are better than those obtained by using the existing DRLG. This is reasonable since the navigation experiments in INS-A suppress the G-sensitive drift effectively. Hence, the optimized DRLG by changing the connection and installation mode in the dithering mechnisim to suppress the G-sensitive drift is a clear improvement for dual-axis rotational INS.

Table 1 Results of all sets of experiments

Experiment item	Error item	Group	INS-A	INS-B
Laboratory static navigation (120 h)	East velocity error/(m/s) (1σ)	1	0.21	0.19
		2	0.25	0.24
		3	0.27	0.20
	North velocity error/(m/s) (1σ)	1	0.25	0.21
		2	0.19	0.25
		3	0.31	0.29
	Longitude error/(′) (Max)	1	**0.92**	**0.51**
		2	**0.87**	**0.35**
		3	**1.06**	**0.42**
	Latitude error/(′) (Max)	1	0.35	0.30
		2	0.42	0.51
		3	0.45	0.37
Vehicle navigation (120 h)	East velocity error/(m/s) (1σ)	1	0.41	0.31
		2	0.23	0.28
		3	0.28	0.35
	North velocity error/(m/s) (1σ)	1	0.31	0.18
		2	0.32	0.32
		3	0.29	0.29
	Longitude error/(′) (Max)	1	**0.94**	**0.47**
		2	**0.98**	**0.43**
		3	**1.23**	**0.52**
	Latitude error/(′) (Max)	1	0.33	0.34
		2	0.46	0.37
		3	0.38	0.45

6. Conclusions

In this paper, the G-sensitive drift of laser gyros is researched by theoretical and simulation analysis. We find that the G-sensitive drift cannot be averaged, and it will cause a slope term of longitude error to increase linearly with time, especially in long-term navigation. On this basis, this paper points out the root cause of this error and designs a new type of dithering mechanism and DRLG. The results of laboratory and vehicle experiments show that the divergence velocity of longitude error can be ef-

fectively reduced by suppressing the G-sensitive drift. The positioning accuracy of the existing DRLG dual-axis rotational INS is improved by nearly 50%. Therefore, the optimization method presented in this paper can be applied to the long-term navigation of various rotational INS or other high-precision INSs.

References

[1] TITTERTON D H, WESTON J L. Strapdown inertial navigation technology. 2nd ed. London: Institution of Engineering and Technology, 2004.

[2] FARRELL J A, BARTH M. The global positioning system and inertial navigation. New York: McGraw-Hill, 1998.

[3] WEI G, YU X D, LONG X W. Novel approach for identifying Z-axis drift of RLG based on GA-SVR model. Journal of Systems Engineering and Electronics, 2014, 25(1): 115–121.

[4] LEVINSON E, HORST J, WILLCOCKS M. The next generation marine inertial navigator is here now. Proc. of the IEEE Position Location and Navigation Symposium, 1994: 121–127.

[5] LEVINSON E, MAJURE R. Accuracy enhancement techniques applied to the marine ring laser inertial navigator (MARLIN). Navigation, 1987, 34: 64–86.

[6] GAO Z Y. Electrostatic gyro technologies. Beijing: Tsinghua University Press, 2004. (in Chinese)

[7] YUAN B L, LIAO D, HAN S L. Error compensation of an optical gyro INS by multi-axis rotation. Measurement Science and Technology, 2012, 23: 025102.

[8] WEI G. Research on some key technologies for double-axis rotation inertial navigation system with mechanically dithered ring laser gyro. Changsha, China: National University of Defense Technology, 2013. (in Chinese)

[9] WANG L, WANG W, ZHANG Q, et al. Self-calibration method based on navigation in high-precision inertial navigation system with fiber optic gyro. Optical Engineering, 2014, 53: 064103.

[10] REN Q, WANG B, DENG Z H, et al. A multi-position self-calibration method for dual-axis rotational inertia navigation system. Sensors and Actuators A: Physical, 2014, 219: 24–31. (in Chinese)

[11] GAO P Y, LI K, WANG L, et al. A self-calibration method for tri-axis rotational inertial navigation system. Measurement Science and Technology, 2016, 27: 115009.

[12] TUUKKA N, JARI K, SAKU S, et al. An enhanced multi-position calibration method for consumer-grade inertial measurement units applied and tested. Measurement Science and Technology, 2010, 21: 105204.

[13] JIANG R, YANG G L, CHEN Y J, et al. Self-calibration of laser gyro g-dependent bias for dual-axis rotational inertial navigation system. Journal of Chinese Inertial Technology, 2017, 25(5): 664–669. (in Chinese)

[14] ZHENG Z C, HAN S L, ZHENG K F. An eight-position self-calibration method for a dual-axis rotational inertial navigation system. Sensors and Actuators A: Physical, 2015, 232: 39–48. (in Chinese)

[15] YU X D, LONG X W. Parametric design of mechanical dither with bimorph piezoelectric actuator for ring laser gyro. International Journal of Applied Electromagnetics and Mechanics, 2015, 47: 305–312.

[16] YU X D, GAO N, XIE Y P, et al. Displacement optimization of the path length control transducer for ring laser gyro using finite element method. International Journal of Applied Electromagnetics and Mechanics, 2015, 49: 327–335.

[17] LEE S H, SHON W H, SUH S W. Piezoelectric actuators for the correction of optical ray path in the operation of laser gyros. International Jounal of Precision Engineering and Manufacturings, 2011, 12: 91–96.

[18] TUO Z H. Study on the dither coupled errors and the error restrain methods for the DRLG SINS. Changsha, China: National University of Defense Technology, 2013. (in Chinese)

[19] YU X D, XIE Y P, XIONG Z Y, et al. Vibration-insensitive optical path length control transducer for ring laser gyro. International Jounal of Precision Engineering and Manufacturings, 2019, 61: 581–591.

[20] MA Y H, YU W, QUAN B X, et al. Influence of path length control mirror on dynamic stability of ring laser gyro. Chinese Journal of Laser, 2017, 44: 0601001. (in Chinese)

[21] LAHHAM J I, WIGENT D J, COLEMAN A L. Tuned support structure for structure-borne noise reduction of inertial navigator with dithered ring laser gyros (RLG). Proc of the IEEE Position Location and Navigation Symposium, 2000: 419–428.

[22] LAHHAM J I, BRAZELL J R. Acoustic noise reduction in the MK49 Ship's inertial navigation system (SINS). Proc of the IEEE Position Location and Navigation Symposium, 1992: 32–39.

[23] YU X D, WEI G, LONG X W, et al. Finite element analysis and optimization of dither mechanism in dithered ring laser gyroscope. International Jounal of Precision Engineering and Manufacturings, 2013, 14: 415–421.

Biographies

YU Xudong was born in 1982. He received his B.S. and Ph.D. degrees in optical engineering from the National University of Defense Technology, in 2001 and 2011, respectively. He is currently an associate researcher in the National University of Defense Technology. His research interests include signal processing, ring laser gyro and inertial navigation system.

E-mail: wind0909@163.com

WANG Zichao was born in 1997. He received his B.S. degree in optical engineering from the National University of Defense Technology, in 2019. He is currently a postgraduate student in the National University of Defense Technology. His research interests include ring laser gyro and inertial navigation system.

E-mail: w731730602@163.com

FAN Huiying was born in 1996. He received his B.S. degree in information and communication engineering from the National University of Defense Technology, in 2018. He is currently working toward his M.S. degree in optical engineering. His research interests include strapdown inertial navigation system and rotation modulation technology.

E-mail: 13404676477@163.com

WEI Guo was born in 1985. He received his B.S. degree in measurement-control technology and instrument from Southeast University and his Ph.D. degree in optical engineering from the National University of Defense Technology, in 2003 and 2013, respectively. He is currently an associate professor in the National University of Defense Technology. His research interests include ring laser gyro, inertial measurement and integrated navigation system.
E-mail: nudtweiguo@163.com

WANG Lin was born in 1987. He received his B.S. and Ph.D. degrees in control science and engineering from the National University of Defense Technology, Changsha, China, in 2013 and 2018, respectively. He is currently an associate researcher in the National University of Defense Technology. His research interests include inertial navigation and integrated navigation system.
E-mail: wanglinshanda@163.com